Multifunctionalized Tumor-Triggered Targeting Theranostic Nanoparticles as a Precision NIR Imaging-Guided Nanoplatform for Photothermal/Photodynamic Therapy

Xu Zhao,* Kang-Kang Zhang, Li-Jian Chen, Zhen-Yu Wang, and Xiu-Ping Yan

Read Online

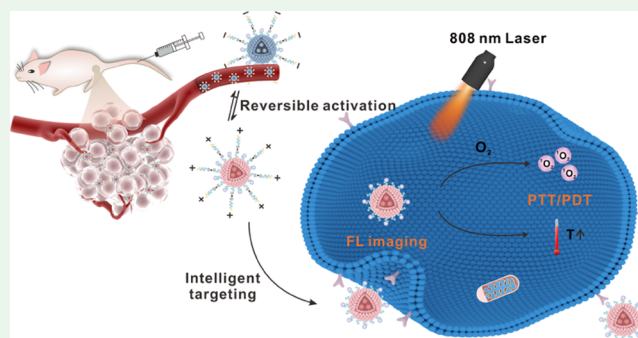ACCESS | Metrics & More | Article Recommendations | Supporting Information

ABSTRACT: Suitable photosensitizers (PSs) are the prerequisite for effective imaging-guided phototherapy. However, traditional PSs have significant limitations, accompanied by unsatisfied tumor targeting ability, poor biocompatibility, and severe side effects. Herein, we report the design of an acid-activated near-infrared (NIR) probe and use it to construct an intelligent theranostic nanoplatform triggered by the tumor microenvironment for tumor-targeting image-guided photothermal and photodynamic therapy (PTT/PDT). First, acid-reversibly responsive brominated asymmetric cyanine 808 (BAC808) with a long-wavelength excitation (808 nm) is designed and synthesized as the tumor-specific NIR fluorescence/photothermal/photodynamic-in-one probe. It integrates acid-activated NIR fluorescence emission, outstanding photothermal conversion efficiency (42.68%), and high $^1O_2$ generation ability ($\Phi_\Delta = 0.10$), enabling effective PDT/PTT with minimized side effects. After encapsulating BAC808 and modification with a charge reversal group and tumor-targeting ligand simultaneously, the multifunctionalized tumor-triggered targeting theranostic nanoparticles (NPs) are fabricated with superior biocompatibility, long circulation time, and tumor-triggered targeting ability. The developed intelligent nanoplatform combines precise tumor targeting ability, specific imaging with a high signal-to-noise ratio, and excellent *in vivo* antitumor activity, making it a potential candidate for anticancer nanodrugs in practical applications.

KEYWORDS: *pH reversible activation, NIR fluorescence imaging, photothermal/photodynamic-in-one probe, intelligent targeting, precision therapy*

INTRODUCTION

As the primary cause of death worldwide, cancer has always been a severe threat to human health and social development.[1] Great efforts have been made to explore novel strategies for cancer diagnosis and treatment in the past few decades.[2−5] However, there remain various barriers in the existing clinical treatments, such as unsatisfied therapeutic effectiveness and severe side effects.[6,7] Therefore, it is critical to explore a novel generation of revolutionary theragnostic strategies to achieve precision diagnosis and efficient treatment of cancer.

Photothermal therapy (PTT) and photodynamic therapy (PDT) are commonly considered as promising treatments for oncotherapy owing to their excellent characteristics of high spatiotemporal precision, negligible invasiveness, and little side effects.[8−10] They generally rely on excited photoactive fluorophores such as photosensitizers (PSs) triggered by the light of a specific wavelength to produce local hyperthermia or reactive oxygen species (ROS), which cause tumor cells to apoptose or even necrose.[11−13] However, single PTT or PDT cannot eradicate tumors due to their inherent defects and concurrent metastasis of tumors, so they are often integrated to construct a multimodal therapy to enhance the therapeutic efficacy.[14−16] More importantly, it is of practical significance to design a PS with fluorescence emission to realize imaging-guided phototherapy, which can diagnose and treat simultaneously and monitor the treatment process in real time.[17−19] Recently, activable PSs are especially attracting attention compared to the traditional "always-on" probes, as they enable precise imaging and more efficient therapeutic treatments for tumors while minimizing side effects.[20−22] Unfortunately, most of the reported PSs are irreversibly activated or limited to short-wavelength excitation, and their therapeutic specificity and efficiency for deep tumors need to be improved.[23,24] Therefore, it is imperative to pursue reversibly activated PSs
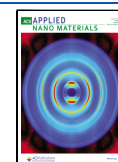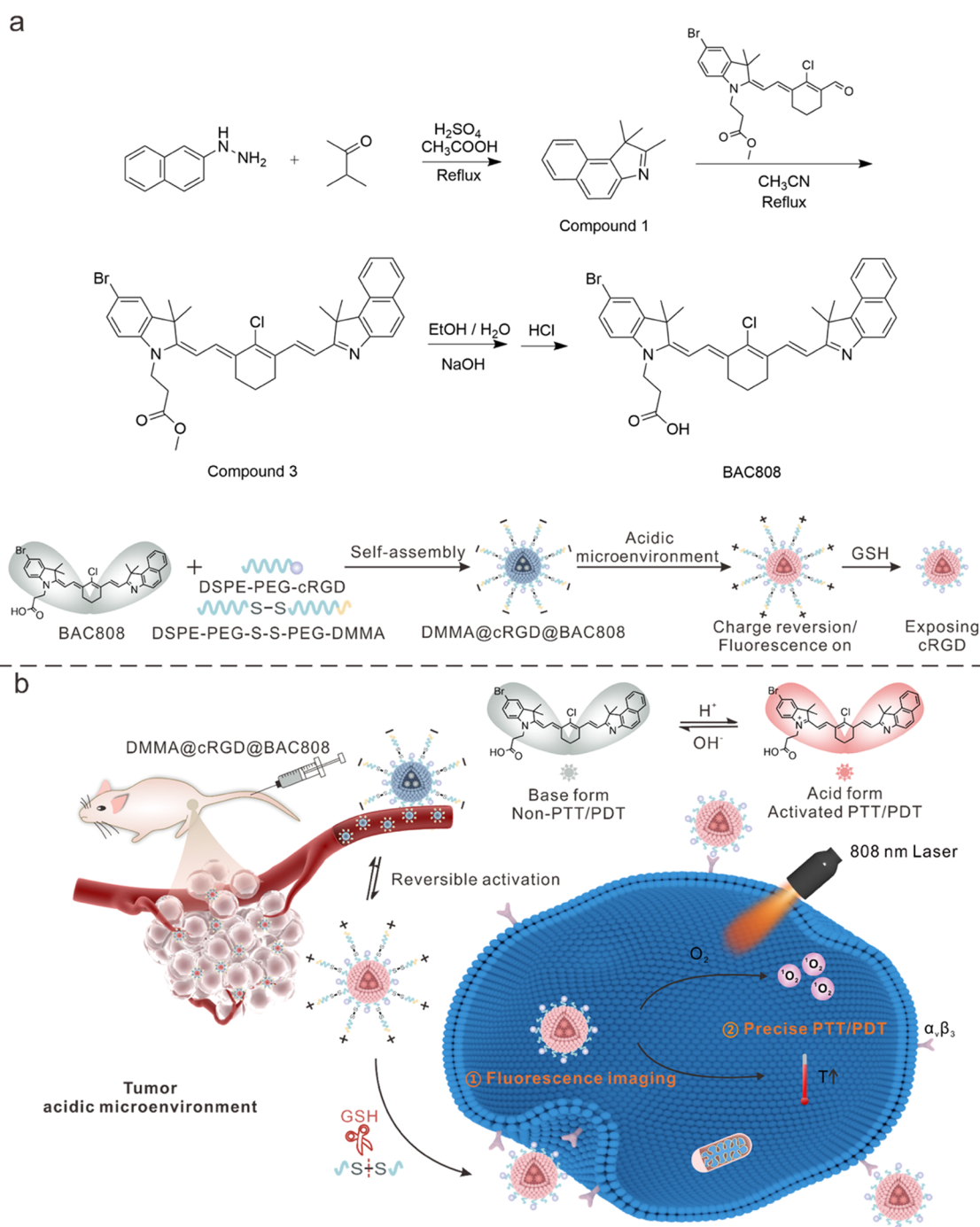
Figure 1. Schematic illustrations of the DMMA@cRGD@BAC808 theranostic nanoplatform. (a) Design and activation mechanism of BAC808 and DMMA@cRGD@BAC808. (b) Illustration of DMMA@cRGD@BAC808 as an acid-reversibly activated PS-based tumor-triggered targeting nanoplatform for precision imaging-guided phototherapy under 808 nm laser irradiation.

relying on near-infrared (NIR) irradiation that can deeply penetrate through tumors with negligible background interference and minimal damage to the adjacent tissues.[25,26]

Biocompatibility and dispersity are other necessary characteristics of clinically ideal PSs that also determine their effectiveness of imaging and therapy *in vivo*.[27] Although several strategies such as attaching charged groups including sulfonate or carboxyl groups to the organic PSs have been designed to improve their solubility, the complicated interactions between the charged PSs and biomolecules hamper their specific accumulation in tumors.[28] In contrast, encapsulation of PSs

into polymetric nanoparticles (NPs) can not only endow PSs with good biocompatibility and dispersity[29,30] but also facilitate their accumulation at tumor sites because of the improved permeability and retention (EPR) effect.[31] In addition, many strategies have been developed to construct a tumor-active targeting nanoplatform for improved imaging and therapeutic effects including specific ligands, charge reversal, pH/GSH sensitivity, and so on.[32-35] Among them, multitarget combination or tumor microenvironment-triggered active targeting strategies have shown great potential against the extremely complicated tumor tissues. However, there are few
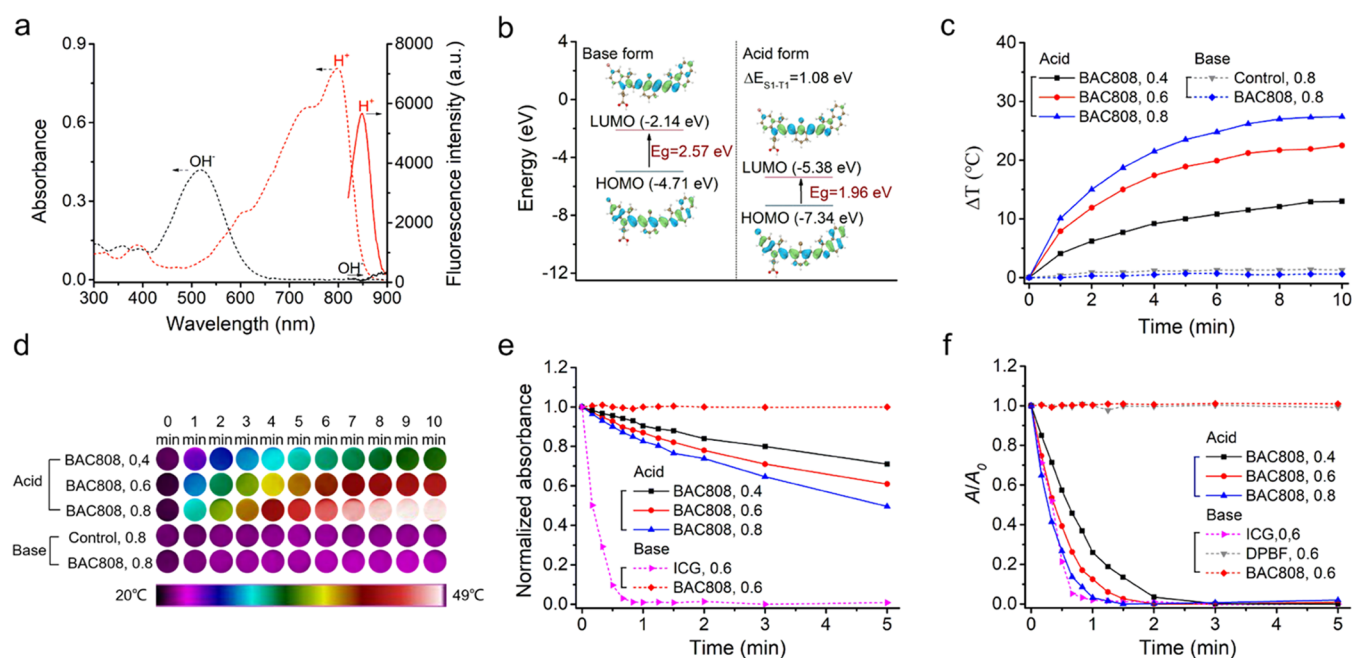
Figure 2. Characterization of BAC808. (a) Fluorescence (solid lines) spectra and UV−vis−NIR absorption (dotted lines) of BAC808 (1×10^{-5} M) in acidic (red lines) and alkaline solutions (black lines). (b) Frontier molecular orbital (HOMO and LUMO) energies of the optimized structures of BAC808 in their ground state (S_0) according to DFT calculations. (c) Temperature changes of BAC808 (1×10^{-5} M) and 50% ethanol as a control for 10 min 808 nm laser irradiation under different power densities (W cm^{-2}). (d) IR thermal images of BAC808 (1×10^{-5} M) and 50% ethanol as a control under different power densities of 808 nm laser irradiation (W cm^{-2}). (e) Effect of irradiation time on the absorbance of BAC808 and ICG (1×10^{-5} M) under different power densities of 808 nm laser irradiation. (f) Time-dependent absorbance of DPBF (A/A_0) at 410 nm with and without BAC808 or ICG (1×10^{-5} M) under different power densities of 808 nm laser irradiation. A_0 represents the original absorbance of DPBF, while A represents the absorbance of DPBF after irradiation for a certain time.

reports on multitarget theragnostic platforms based on tumor microenvironment triggering. Therefore, it is of practical significance to develop a multitargeting reversibly activated theranostic nanoplatform triggered by the tumor microenvironment, which can prolong the blood circulation and increase the accumulation of drugs in tumor sites.

Herein, we report the design and synthesis of novel pH-reversibly responsive NIR fluorescent/PTT/PDT-in-one probe BAC808 and develop a BAC808-loaded tumor-triggered multi-intelligent targeting theranostic nanoplatform for precise tumor-targeted imaging-guided synchronous phototherapy. Brominated asymmetric cyanine (BAC808) with a long-wavelength excitation (808 nm) is designed as a pH-activated NIR fluorescent/PTT/PDT-in-one agent for specific tumor imaging and high-efficient PTT/PDT therapy. Furthermore, DSPE-PEG$_{2000}$-S−S-PEG$_{2000}$-DMMA and DSPE-PEG$_{2000}$-cRGD are introduced to encapsulate BAC808 into NPs, endowing the obtained NPs with dual targeting of charge reversal and stealth intelligence triggered by the tumor microenvironment as well as good biocompatibility and dispersity. The designed DMMA@cRGD@BAC808 theranostic nanoplatform presents tumor-targeted imaging and superior anticancer capabilities with outstanding tumor specificity and negligible side effects, which is regarded as a potential candidate in future practical applications.

■ RESULTS AND DISCUSSION

Design of the DMMA@cRGD@BAC808 Theranostic Nanoplatform. The design strategy and fabrication of the DMMA@cRGD@BAC808 theranostic platform for precision tumor-targeting imaging-guided PTT/PDT synergistic therapy

are shown in Figure 1. A fluorescent/PTT/PDT-in-one molecule BAC808 is first designed and synthesized as the pH-reversibly activated NIR PSs for precise tumor imaging-guided synchronous PTT/PDT. To enable tumor-specific activation in the acidic environment, the unsubstituted *N* atom was retained in the indole ring of BAC808 and served as the specific recognition site. At the same time, the introduction of the aromatic ring red-shifts the fluorescence excitation of BAC808 due to the enlarged π-conjugated system to better match with the 808 nm laser light source, which contributes to the enhanced effectiveness of NIR fluorescence imaging and phototherapy under the irradiation of an 808 nm laser.[36] In addition, to endow BAC808 with good hydrophilicity and biocompatibility *in vivo*, the corresponding DMMA@cRGD@BAC808 NPs were prepared using DSPE-PEG$_{2000}$-S−S-PEG$_{2000}$-DMMA and DSPE-PEG$_{2000}$-cRGD as the polymer matrix by a coprecipitation method.[37] The as-prepared DMMA@cRGD@BAC808 NPs represent a negative charge under normal physiological conditions, which are favorable to prolong the blood circulation until its charge reversion when arriving at the tumor acidic microenvironment via leaky blood vessels.[38] Because of their opposite charge attraction, these nanoparticles accumulate in tumors and the disulfide bond (S−S) of DSPE-PEG$_{2000}$-S−S-PEG$_{2000}$-DMMA is subsequently cleaved by overexpressed GSH in the tumor microenvironment. Then, the exposed cRGD on the surface of DMMA@cRGD@BAC808 can interact with the plasma membrane of cancer cells via specific recognition with $\alpha_\nu\beta_3$ integrin, endowing DMMA@cRGD@BAC808 with tumor active targeting capability.[39] Meanwhile, BAC808 is changed from the base form to the acid form with the activation of
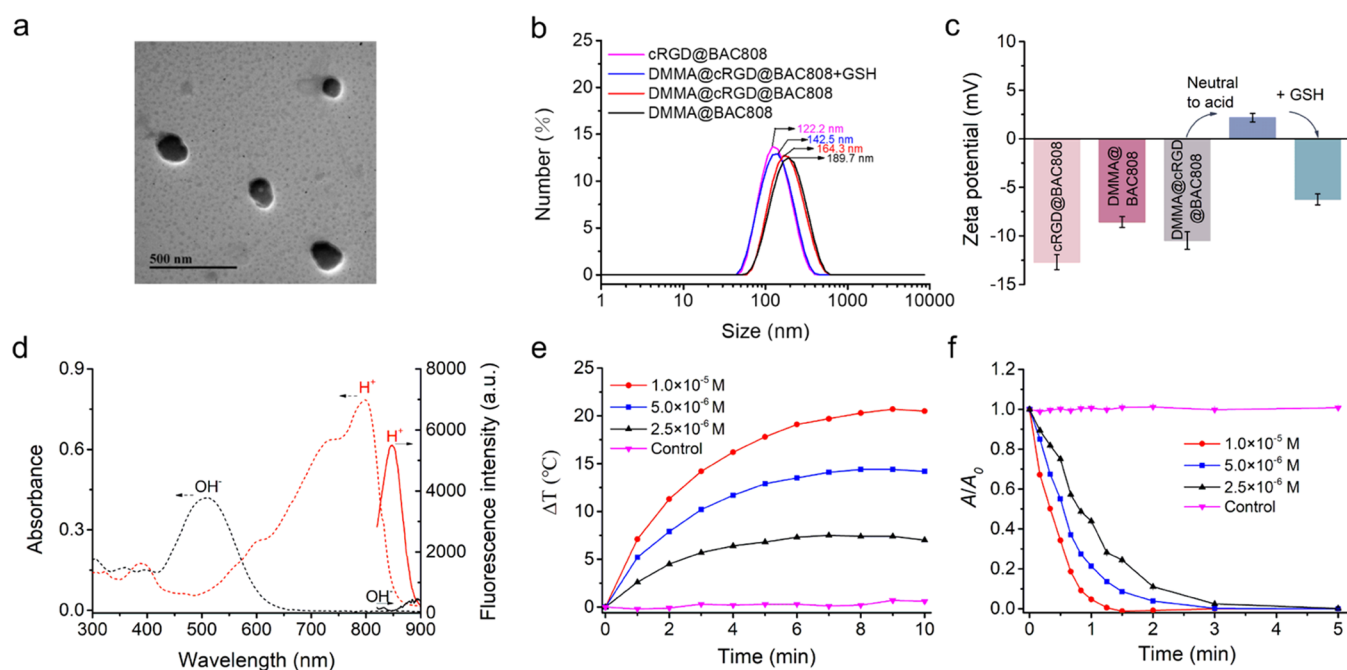
Figure 3. Characterization of DMMA@cRGD@BAC808. (a) TEM images of DMMA@cRGD@BAC808. (b) Hydrodynamic diameter distribution of cRGD@BAC808, DMMA@BAC808, DMMA@cRGD@BAC808, and DMMA@cRGD@BAC808 treated with 10 mM GSH. (c) ζ potentials of cRGD@BAC808, DMMA@BAC808, and DMMA@cRGD@BAC808 treated with 10 mM GSH or not. (d) UV−vis−NIR absorption (dotted lines) and fluorescence (solid lines) spectra of DMMA@cRGD@BAC808 (1×10^{-5} M) in acidic (red lines) and alkaline solutions (black lines). (e) Photothermal performance of DMMA@cRGD@BAC808 at various concentrations of acidic solutions and its alkaline solution (1×10^{-5} M) as a control during a 10 min exposure to the 808 nm laser (0.6 W cm^{-2}). (f) Time-dependent absorbance of DPBF (A/A_0) at 410 nm with various concentrations of acidic DMMA@cRGD@BAC808 and its alkaline solution (1×10^{-5} M) as a control under 0.6 W cm^{-2} of 808 nm laser irradiation. A_0 represents the original absorbance of DPBF, while A represents the absorbance of DPBF after irradiation for a certain time.

fluorescence, photothermal, and photodynamic properties. As such, the as-designed DMMA@cRGD@BAC808 nanoplatform enables intelligent tumor-targeting imaging-guided precision phototherapy under the 808 nm laser irradiation.

Preparation and Characterization of BAC808. BAC808 was successfully prepared via the synthetic routes outlined in Figure 1a, and the detailed procedures could be obtained in the SI. The structures of BAC808 and the significant intermediates during the synthesis were confirmed by the nuclear magnetic resonance, high-resolution mass spectra, and Fourier transform infrared (FT-IR) spectra (Figures S1−S10). BAC808 holds a characteristic absorption peak at ca. 518 nm in alkaline medium (ethanol/water, 5/5 v/v), while it shows a new shoulder band at ca. 808 nm in acidic medium with the disappearance of its absorption band at 518 nm (Figure 2a). According to density functional theory (DFT) calculations, the gap (E_g) between the lowest occupied molecular orbital (LUMO) and the highest unoccupied molecular orbital (HOMO) of BAC808 is narrowed owing to the protonation of unsubstituted N atoms in the indole ring, resulting in the difference of its optical properties in acidic and alkaline solutions (Figure 2b). Owing to the intramolecular charge transfer during the protonation of N atoms of the indole ring, the activated BAC808 under acidic conditions exhibits a NIR absorption and emission, with the maximum wavelength at 808 and 850 nm, respectively. Fluorescence titration experiments were used to determine that the pK_a and pH-sensitive intervals of BAC808 are, respectively, 5.75 and 4.0−7.5 (Figures S11 and S12).

In addition, common ionic biocomponents such as K$^+$, Na$^+$, Mg^{2+}, and Ca^{2+} exhibited no interference to the pH reversible

response properties of BAC808 even at the concentration of 0.1 M (Figure S13). These results all conclude that the as-synthesized BAC808 possesses pH-reversibly responsive properties and pH-sensitive intervals consistent with the tumor acidic microenvironment, which can serve as a specific activated PS for precise imaging-guided phototherapy of tumors.[40]

Photothermal and photodynamic properties of BAC808 were further studied. After being excited to the S1 state under acidic conditions, the activated BAC808 would consume its energy through a nonradiative decay pathway, leading to the released heat (Figure 2b). Meanwhile, the BAC808 at the excited state would also cause an enhanced singlet-to-triplet intersystem crossing (ISC) due to the charge transfer and heavy atom effect, further producing singlet oxygen (^{1}O$_2$) through energy transfer for inducing efficient PDT. These results indicate that BAC808 is promising for effective PTT and PDT in the acidic tumor microenvironment. Thus, the acid-activated photothermal properties of BAC808 were first investigated using various power densities of an 808 nm laser as the excitation source (Figure 2c). The temperatures of BAC808 in acidic solutions upon 0.4, 0.6, and 0.8 W cm^{-2} of laser irradiation (808 nm, 10 min) increased 13.0, 22.5, and 27.4 °C, respectively. The BAC808 in acidic solutions also exhibited exposure time- and concentration-dependent hyperthermia (Figures 2c,d and S14). In contrast, the solution alone and BAC808 in the alkaline environment as the control groups did not exhibit any temperature change during the 10 min irradiation even when the power density was up to 0.8 W cm^{-2} (Figure 2c,d). The superior photothermal activity of BAC808 was also demonstrated by its photothermal conversion

efficiency under 0.6 W cm^{-2} of 808 nm irradiation, which was determined to be 42.68% (Figure S15). These results indicate that BAC808 could exhibit desirable photothermal capabilities only when activated by the acidic environment, making it competent for tumor-specific PTT. Furthermore, BAC808 shows more excellent photostability than that of indocyanine green (ICG) as the typical NIR dye, especially at pH 7.4 (Figure 2e), guaranteeing its stability in *in vivo* blood circulation. Together with the photothermal efficiency and photostability capabilities of BAC808, 0.6 W cm^{-2} was chosen as the optimal laser power in the following experiments.

The photodynamic property of BAC808 was investigated subsequently with 1,3-diphenylisobenzofuran (DPBF) as the indicator of singlet oxygen ($^1O_2$). Almost no change in the absorption spectra of DPBF was observed with and without BAC808 in alkaline solutions after 5 min of 808 nm laser irradiation (0.6 W cm^{-2}) (Figures 2f and S16). In contrast, when irradiating the acidic BAC808 solutions with different power densities of the 808 nm laser, a 100% decrease of the initial absorbance of DPBF at 410 nm was observed only in 3 min, confirming the efficient generation of $^1O_2$ (Figures 2f and S17). Besides, the $^1O_2$ generation efficiency of BAC808 appeared to be concentration-, power density-, and exposure time-dependent (Figures 2f and S18). The $^1O_2$ generation ability of ICG was also measured under 0.6 W cm^{-2} of 808 nm irradiation for comparison (Figures 2f, S19 and S20). The singlet oxygen quantum yield (Φ_Δ) of activated BAC808 was then calculated to be 0.10 when using DPBF and 2,7-dichlorodihydrofluorescein diacetate (DCFH-DA) as the $^1O_2$ indicator, revealing a comparable capacity for $^1O_2$ generation to ICG (Φ_Δ = 0.14).[41] The efficient generation of $^1O_2$ for BAC808 only in the acidic environment provides BAC808 with great potential for tumor-specific PDT. In conclusion, the outstanding PTT/PDT properties of acid-reversibly activated BAC808 make it qualify as an intelligent PTT/PDT-in-one agent for tumor-targeting precision phototherapy.

Preparation and Characterization of the DMMA@cRGD@BAC808 Theranostic Nanoplatform. Considering the excellent acid-reversibly activated properties of BAC808, a microenvironment-triggered tumor-active targeting theranostic nanoplatform was proposed for NIR fluorescence imaging-guided precision PTT/PDT in this study. To this end, the BAC808-based NPs were fabricated by encapsulating BAC808 in the hydrophobic cavity of DSPE-PEG$_{2000}$-S—S-PEG$_{2000}$-DMMA and DSPE-PEG$_{2000}$-cRGD to prolong their blood circulation, improve their tumor targeting ability, and enhance their biocompatibility. The appearance of the characteristic bands at 1704 cm^{-1} (—C≡C— stretching vibration of DMMA) and 1643 cm^{-1} (—CONH— vibration of cRGD) in the FT-IR spectrum confirmed the successful preparation of DMMA@cRGD@BAC808 (Figure S21). The prepared DMMA@cRGD@BAC808 has a spherical shape with an average diameter and hydrodynamic diameter of around 131.0 ± 8.9 and 164.3 ± 7.4 nm, respectively (Figure 3a,b), which are beneficial for avoiding the clearance of the reticuloendothelial system (RES) during the blood circulation to accumulate tumor sites through the EPR effect. The ζ potential is also essential to trace the successful fabrication of DMMA@cRGD@BAC808. Meaningfully, the DMMA@cRGD@BAC808 showed negative potential at −10.47 ± 0.89 mV under the neutral conditions, suggesting the potential capacity for prolonging the circulation time in blood (Figure 3c). As the environmental pH reduced, the ζ potential of

DMMA@cRGD@BAC808 turned into a positive charge at 2.17 ± 0.44, revealing its charge reversal target ability owing to the hydrolysis of DMMA and protonation of the exposed amino terminal under acidic conditions, which contributes to its accumulation at the sites of tumors. The encapsulation efficiency (EE) was also calculated to be 88.4% according to the standard curve of BAC808 (Figure S22). Furthermore, the as-prepared DMMA@cRGD@BAC808 has satisfactory stability as confirmed by the negligible changes of the hydrodynamic diameter after storage in water and phosphate-buffered saline (PBS) with 10% fetal bovine serum (FBS) for two weeks (Figure S23).

To verify the microenvironment-triggered tumor targeting ability of DMMA@cRGD@BAC808, DMMA@BAC808 and cRGD@BAC808 were also prepared for comparison in a similar procedure using DSPE-PEG$_{2000}$-S—S-PEG$_{2000}$-DMMA and DSPE-PEG$_{2000}$-cRGD, respectively. In FT-IR spectra, the typical stretching vibration peaks of DMMA@BAC808 and cRGD@BAC808 appeared at 1704 cm^{-1} (—C≡C— group of DMMA) and 1643 cm^{-1} (—CONH— unit of cRGD) with the hydrodynamic size were 189.7 ± 9.1 nm and 122.2 ± 10.9 nm (Figures 3b and S24). Furthermore, the ζ potentials of DMMA@BAC808 and cRGD@BAC808 were −8.57 ± 0.56 and −12.70 ± 0.78, respectively, which evidenced the successful modification with DSPE-PEG$_{2000}$-S—S-PEG$_{2000}$-DMMA and DSPE-PEG$_{2000}$-cRGD (Figure 3c).

To confirm the exposure of cRGD after the disulfide bond of DMMA@cRGD@BAC808 being cleaved by GSH under the tumor microenvironment, the hydrodynamic diameter, ζ potential, and FT-IR spectra of DMMA@cRGD@BAC808 after treated with 10 mM GSH were also measured. The average hydrodynamic diameter of DMMA@cRGD@BAC808 NPs treated after 10 mM GSH was about 21.8 nm lower than that of DMMA@cRGD@BAC808 NPs untreated, confirming that GSH could indeed cleave the disulfide bond of DSPE-PEG$_{2000}$-S—S-PEG$_{2000}$-DMMA (Figure 3b). Meanwhile, the ζ potential changed to −6.24 ± 0.57 mV, while the typical infrared stretching vibration band of DMMA at 1704 cm^{-1} disappeared, which also indicates that cRGD is exposed with the disappearance of DMMA. (Figure 3c and S24).

The optical properties of DMMA@cRGD@BAC808 were further evaluated (Figure 3d). In comparison with bare BAC808, the DMMA@cRGD@BAC808 in the alkaline solution showed a slightly blue-shifted absorption peak due to the aggregation of PSs when they were encapsulated into NPs. However, no noticeable change was observed in its absorption and fluorescence spectra when dispersed in acidic solutions, proving that the DMMA@cRGD@BAC808 still holds outstanding acid-reversibly responsive optical properties for tumor-specific imaging-guided phototherapy.

***In Vitro* PTT/PDT Performance of DMMA@cRGD@BAC808.** Acid-responsive photothermal activity of DMMA@cRGD@BAC808 was first evaluated by exposing to 10 min of 808 nm laser irradiation (0.6 W cm^{-2}). The temperatures of DMMA@cRGD@BAC808 in acidic solutions increased obviously with its concentration as well as the irradiation time (Figures 3e and S25). In contrast, the alkaline solution of DMMA@cRGD@BAC808 did not induce any temperature increase under the same laser irradiation, demonstrating that the DMMA@cRGD@BAC808 holds prominent acid-activated photothermal effects.

The $^1O_2$ generation activity of DMMA@cRGD@BAC808 was tested subsequently. Upon laser irradiation (808 nm, 0.6
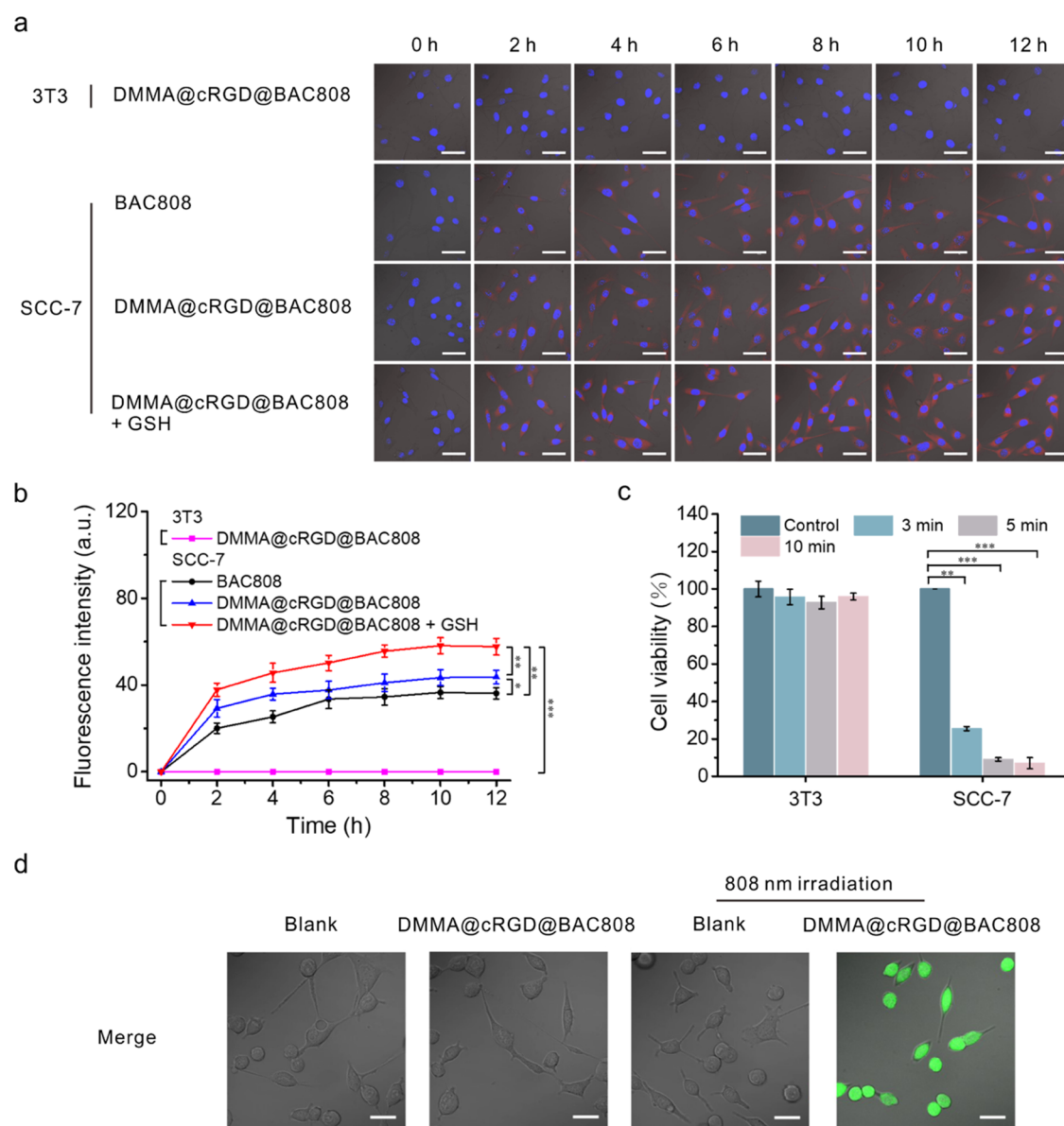
Figure 4. Cell internalization and *in vitro* PTT/PDT effect of DMMA@cRGD@BAC808. (a) Cell internalization and cell imaging of BAC808, DMMA@cRGD@BAC808, and DMMA@cRGD@BAC808 with 5 μM GSH toward 3T3 and SCC-7 cells (scale bar, 50 μm). (b) Fluorescence intensity of cells incubated with BAC808, DMMA@cRGD@BAC808, and DMMA@cRGD@BAC808 with 5 μM GSH for different times. (c) Cell viability of DMMA@cRGD@BAC808 under different irradiation times of an 808 nm laser (0.6 W cm^{-2}) against 3T3 and SCC-7 cells. The control refers to 808 nm laser irradiation alone for 10 min. Data were presented as the mean $\pm$ SD ($n = 5$). *$P < 0.05$, **$P < 0.01$, and ***$P < 0.001$. (d) ROS production mediated by DMMA@cRGD@BAC808 (1.0×10^{-5} M) upon irradiation (808 nm, 0.6 W cm^{-2}, 5 min) as indicated by the fluorescence of DCFH (scale bar, 30 μm).

W cm^{-2}, 5 min), the $^1O_2$ generation of DMMA@cRGD@BAC808 was monitored using DPBF as an indicator. As expected, a rapid and considerable decline of the absorbance of DPBF was observed with acidic solutions of DMMA@cRGD@BAC808, confirming the efficient $^1O_2$ generation (Figures 3f and S26). In comparison, the absorption spectra of DPBF remained unchanged with time for the alkaline solution of DMMA@cRGD@BAC808, confirming that no $^1O_2$ was produced under the same treatment. The above-mentioned results indicate that the DMMA@cRGD@BAC808 holds a great potential for tumor-specific phototherapy.

Cell Targeting NIR Imaging and PTT/PDT of DMMA@cRGD@BAC808. The *in vitro* tumor-targeted NIR fluorescence imaging and PTT/PDT effect of DMMA@cRGD@

BAC808 were confirmed with SCC-7 cells as model tumor cells and 3T3 normal cells as the negative control. The MTT assay was carried out first to assess the dark cytotoxicity of both DMMA@cRGD@BAC808 and bare BAC808 toward 3T3 cells. Compared to BAC808, the DMMA@cRGD@BAC808 appeared to have no obvious cytotoxicity to 3T3 cells, and the cell viabilities were all kept over 90%, even though the concentration was up to 50 μM (Figure S27). These results indicate that encapsulation of BAC808 into NPs effectively improves its biocompatibility and is more conducive to subsequent biological applications.

In order to investigate the cellular uptake and specific imaging of tumor cells, 10 μM DMMA@cRGD@BAC808 was incubated with 3T3 and SCC-7 cells and monitored by
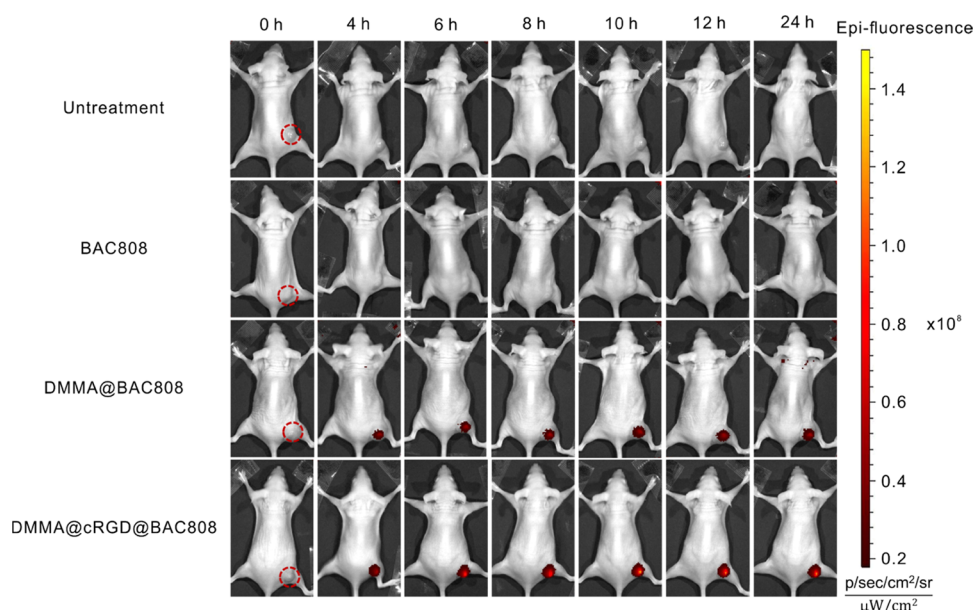
Figure 5. *In vivo* fluorescence images of SCC-7 tumor-bearing mice throughout time after intravenous injection with BAC808, DMMA@BAC808, and DMMA@cRGD@BAC808.

confocal laser scanning microscopy (CLSM). As depicted in Figure 4a, after incubation for different times, red signals denoting the fluorescent probe in SCC-7 cells were observed to gradually increase and reached the maximum at 10 h, indicating that the probe was internalized and gradually accumulated in SCC-7 cells. In comparison, no fluorescence signal was detected in 3T3 cells because their neutral conditions could not activate BAC808, further validating the excellent tumor-specific imaging capability of BAC808. Besides, the fluorescence signal of SCC-7 cells treated with DMMA@cRGD@BAC808 was slightly higher than that of bare BAC808 with the same concentration, suggesting that the strategy of encapsulating BAC808 into NPs does not change its optical properties and is favorable for its endocytosis. It was noteworthy that much stronger fluorescence of 5 μM GSH-pretreated SCC-7 cells coincubated with DMMA@cRGD@BAC808 was also observed compared to the SCC-7 cell group with about a 1.3-fold increase of the mean fluorescence intensity (MFI) (Figure 4b). This was attributed to the increased internalization of DMMA@cRGD@BAC808 in GSH-pretreated SCC-7 cells since the exposed cRGD peptide in the presence of GSH could specifically bind to the $\alpha\nu\beta3$ integrin receptor highly expressed on SCC-7 cell membranes.[42] These results confirmed that the as-prepared DMMA@cRGD@BAC808 could obviously promote its specific targeting ability and cellular uptake toward SCC-7 cells under the tumor microenvironment for further specific tumor-targeted NIR imaging *in vivo*.

The PTT/PDT efficiency of DMMA@cRGD@BAC808 was then evaluated toward tumor cells (SCC-7, pH 6.5) and normal cells (3T3, pH 7.4). As illustrated in Figure 4c, less than 10% cell viability was observed for SCC-7 cells treated with DMMA@cRGD@BAC808 under 808 nm laser irradiation (0.6 W cm^{-2}) for only 5 min, confirming the apparent cytotoxicity of DMMA@cRGD@BAC808 against the tumor cells. In contrast, a negligible cell cytotoxicity (ca. 90% cell viability) was observed for 3T3 cells when exposing to 0.6 W cm^{-2} 808 nm irradiation even for 10 min. Similar results were likewise acquired from the calcein-AM/PI staining experiments

(Figure S28). The intracellular ROS generation was also detected using DCFH-DA as the indicator (Figure 4d). Obvious green fluorescence was monitored from the SCC-7 cells only in the group conducted with 808 nm irradiation (0.6 W cm^{-2}, 5 min) after being cultured with DMMA@cRGD@BAC808 for 10 h, indicating significant ROS generation only under this condition. All of these data convincingly verify that the DMMA@cRGD@BAC808 could merely be activated under the tumor acidic microenvironment and achieved outstanding PTT/PDT without toxicity to normal cells.

***In Vivo* Tumor Targeting NIR Imaging and Precision Therapy.** Inspired by its prominent performance *in vitro*, the DMMA@cRGD@BAC808 was subsequently applied for *in vivo* tumor targeting NIR imaging and image-guided precision PTT/PDT with SCC-7 tumor-bearing mice. All animal experiments were conducted strictly in compliance with the Guidelines for Care and Use of Laboratory Animals of Jiangnan University and approved by the Animal Ethics Committee of Jiangnan University, People's Republic of China (JN. No 20220930b0241210[406]). To guarantee its safety for *in vivo* application, the compatibility of DMMA@cRGD@BAC808 with blood was first estimated via hemolysis assay. The hemolysis rates of red blood cells were all less than 1% among these groups incubated with DMMA@cRGD@BAC808 at different concentrations, indicating its favorable hemocompatibility (Figure S29). The *in vivo* imaging performance was then investigated via the following four groups: (1) untreatment and (2−4) intravenous injection with BAC808, DMMA@BAC808, and DMMA@cRGD@BAC808. As depicted in Figure 5, no fluorescence signal could be detected at the tumor site after injecting BAC808 because the BAC808 alone lacks the targeting ability and was quickly metabolized out of the body via blood circulation. In comparison, significant fluorescence occurred at the tumor site after intravenous injection with DMMA@BAC808 or DMMA@cRGD@BAC808, gradually increased within 10 h, and maintained detectability for at least 24 h. The reason is that compared with organic small-molecule fluorophores, the nanoplatform constructed using DSPE-PEG$_{2000}$-S-S-PEG$_{2000}$-
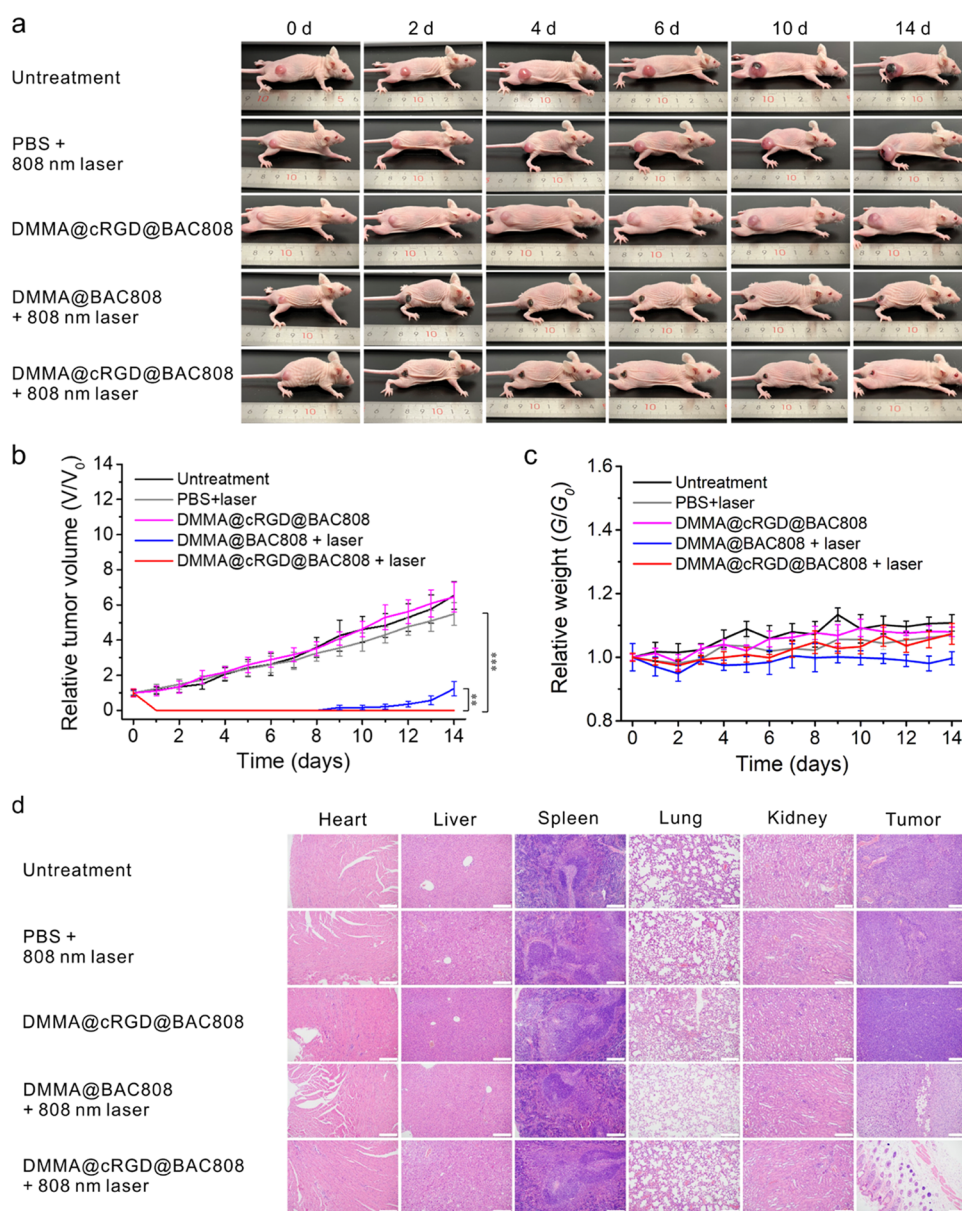
Figure 6. *In vivo* PTT/PDT of DMMA@cRGD@BAC808 in SCC-7 tumor-bearing mice models. (a) Representative images of the tumor-bearing mice of various groups during the PTT/PDT treatment. (b) Relative tumor volume changes in mice after the PTT/PDT compared to original tumor volumes. V and V_0 are the volumes of the tumor at a certain day after treatment and before treatment, respectively. Data were presented as the mean $\pm$ SD ($n = 3$). **$P < 0.01$ and ***$P < 0.001$. (c) Body weight changes of mice during the PTT/PDT treatment process. G_0 is the initial weight of mice, while G is the weight at a certain day after the PTT/PDT treatment of different groups. (d) H&E staining of the major organs and tumor tissues of mice after the therapy (scale bar, 200 μm). Center values and error bars are defined as mean and s.d., respectively ($n = 3$).

DMMA could simultaneously prolong its blood circulation and improve its ability to target tumors due to the EPR effect of nanoparticles and the charge reversal ability of DMMA. Therefore, 10 h after injection was chosen as the optimal time for 808 nm irradiation in the follow-up therapy. Furthermore, the fluorescence intensity in the tumor sites of SCC-7 tumor-bearing mice treated with DMMA@cRGD@BAC808 exhibited a 1.3-fold increase compared with that treated with DMMA@BAC808 because the exposed cRGD only in the tumor microenvironment increased the ability of DMMA@cRGD@BAC808 to bind with cancer cells, resulting in the enhanced cellular uptake (Figure S30). Noteworthily, no fluorescence signal was observed in all other tissues and organs of mice in the experimental groups, verifying the precision *in*

vivo tumor targeting imaging ability of the prepared nanoplatform.

To investigate the *in vivo* metabolism and biodistribution of DMMA@cRGD@BAC808, tumors and major organs of mice after intravenous injection for different times were harvested for *ex vivo* imaging. The tumor, liver, spleen, and kidney samples exhibited notable NIR fluorescence signals, and little appreciable signal was monitored in other organs (Figure S31). Furthermore, the fluorescence intensity in the tumor and organs gradually decreased over time and completely disappeared after 10 days, indicating that DMMA@cRGD@BAC808 could be metabolized completely within 10 days *in vivo*.

The *in vivo* antitumor effect of DMMA@cRGD@BAC808 was then evaluated (Figure 6). After 10 h of intravenous

injection of DMMA@cRGD@BAC808 or DMMA@BAC808, the experimental groups of SCC-7 tumor-bearing mice were exposed to 808 nm laser irradiation (0.6 W cm^{-2}, 5 min). Meanwhile, tumor-bearing mice in other groups untreated or injected with DMMA@cRGD@BAC808 alone or treated with PBS combined with the same laser irradiation were set as the control.

During two weeks of the therapeutic period, the tumor volume in the DMMA@cRGD@BAC808 group without laser irradiation increased exponentially, same as that in the untreated and PBS with laser irradiation treatment groups, indicating that neither laser irradiation alone nor DMMA@cRGD@BAC808 alone could suppress tumor growth. In stark contrast, markedly reduced tumor volume was observed in DMMA@BAC808- and DMMA@cRGD@BAC808-treated groups with 808 nm irradiation. Especially, the tumors for DMMA@cRGD@BAC808 with 808 nm irradiation were utterly eliminated even in the late stage, while the tumors for DMMA@BAC808 under the same treatment appeared to recur during two weeks (Figure 6b). The superior therapeutic effect of DMMA@cRGD@BAC808 compared with that of DMMA@BAC808 was attributed to that the tumor micro-environment-triggered exposure of cRGD increased its accumulation in tumors. Furthermore, there were no abnormal body weight loss and noticeable damage of the main organs in both experimental and control groups, validating the negligible toxicity of DMMA@cRGD@BAC808 (Figure 6c,d). All these results convincingly demonstrate that the synthesized DMMA@cRGD@BAC808 was suitable for microenvironment-triggered tumor-targeting therapy by a single intravenous injection under short-time laser irradiation with ideal therapeutic effects without noticeable adverse effects.

■ CONCLUSIONS

In conclusion, we have successfully designed a novel NIR fluorophore, BAC808, and encapsulated it into NPs to develop an intelligent theranostic nanoplatform (DMMA@cRGD@BAC808) for precision tumor-targeting imaging-guided synergistic PDT and PTT. The synthesized acid-reversibly activated probe BAC808 exhibited high absorption at a long wavelength (808 nm), which is beneficial to improve its $^{1}O_2$ production capacity and photothermal activity under 808 nm laser irradiation when activated by the tumor acidic environment. Functionalization with DSPE-PEG$_{2000}$-S−S-PEG$_{2000}$-DMMA and DSPE-PEG$_{2000}$-cRGD not only endows the corresponding DMMA@cRGD@BAC808 with tumor-triggered charge reversal and incognito active targeting capacity but also makes it qualify as an intelligent theranostic nanoplatform with favorable hydrophilicity, stability, and biocompatibility. This study provides new insights into the design of intelligent theranostic nanoplatforms based on small-molecule fluorophores, overcomes the nonspecific damage in the traditional "always-on" therapeutic platforms, and provides new candidate probes for clinical therapeutic applications.

■ ASSOCIATED CONTENT

Ⓢ Supporting Information

The Supporting Information is available free of charge at https://pubs.acs.org/doi/10.1021/acsanm.3c01473.

Chemicals and materials, instrumentation, synthetic procedures, and experimental details (PDF)

■ AUTHOR INFORMATION

Corresponding Author

Xu Zhao − *State Key Laboratory of Food Science and Technology, Jiangnan University, Wuxi 214122, China; International Joint Laboratory on Food Safety and School of Food Science and Technology, Institute of Analytical Food Safety, Jiangnan University, Wuxi 214122, China;* ⓞ orcid.org/0000-0001-8000-9045; Email: zhaoxu2017@jiangnan.edu.cn

Authors

Kang-Kang Zhang − *State Key Laboratory of Food Science and Technology, Jiangnan University, Wuxi 214122, China; International Joint Laboratory on Food Safety and School of Food Science and Technology, Institute of Analytical Food Safety, Jiangnan University, Wuxi 214122, China;* ⓞ orcid.org/0009-0006-5192-4133

Li-Jian Chen − *State Key Laboratory of Food Science and Technology, Jiangnan University, Wuxi 214122, China; International Joint Laboratory on Food Safety and School of Food Science and Technology, Institute of Analytical Food Safety, Jiangnan University, Wuxi 214122, China;* ⓞ orcid.org/0000-0001-8671-8766

Zhen-Yu Wang − *School of Environment and Civil Engineering, Institute of Environmental Processes and Pollution Control, Jiangnan University, Wuxi 214122, China;* ⓞ orcid.org/0000-0002-5114-435X

Xiu-Ping Yan − *State Key Laboratory of Food Science and Technology, Jiangnan University, Wuxi 214122, China; International Joint Laboratory on Food Safety and School of Food Science and Technology, Institute of Analytical Food Safety, Jiangnan University, Wuxi 214122, China;* ⓞ orcid.org/0000-0001-9953-7681

Complete contact information is available at:
https://pubs.acs.org/10.1021/acsanm.3c01473

Notes

The authors declare no competing financial interest.

■ ACKNOWLEDGMENTS

■ REFERENCES

(1) Bray, F.; Ferlay, J.; Soerjomataram, I.; Siegel, R. L.; Torre, L. A.; Jemal, A. Global Cancer Statistics 2018: GLOBOCAN Estimates of Incidence and Mortality Worldwide for 36 Cancers in 185 Countries. *CA Cancer J. Clin.* **2018**, *68*, 394−424.

(2) Xu, H.; Ohulchanskyy, T. Y.; Yakovliev, A.; Zinyuk, R.; Song, J.; Liu, L.; Qu, J.; Yuan, Z. Nanoliposomes Co-Encapsulating CT Imaging Contrast Agent and Photosensitizer for Enhanced, Imaging Guided Photodynamic Therapy of Cancer. *Theranostics* **2019**, *9*, 1323−1335.

(3) Ding, Y.; Dai, Y.; Wu, M.; Li, L. Glutathione-Mediated Nanomedicines for Cancer Diagnosis and Therapy. *Chem. Eng. J.* **2021**, *426*, No. 128880.

(4) Yao, S.; Liu, Z.; Li, L. Recent Progress in Nanoscale Covalent Organic Frameworks for Cancer Diagnosis and Therapy. *Nano-Micro Lett.* **2021**, *13*, No. 176.

(5) Llop, J.; Lammers, T. Nanoparticles for Cancer Diagnosis, Radionuclide Therapy and Theranostics. *ACS Nano* **2021**, *15*, 16974−16981.

(6) Li, X.; Lee, S.; Yoon, J. Supramolecular Photosensitizers Rejuvenate Photodynamic Therapy. *Chem. Soc. Rev.* **2018**, *47*, 1174−1188.

(7) Li, X.; Kim, J.; Yoon, J.; Chen, X. Cancer-Associated, Stimuli-Driven, Turn on Theranostics for Multimodality Imaging and Therapy. *Adv. Mater.* **2017**, *29*, No. 1606857.

(8) Wu, W.; Bazan, G. C.; Liu, B. Conjugated-Polymer-Amplified Sensing, Imaging, and Therapy. *Chem* **2017**, *2*, 760−790.

(9) Celli, J. P.; Spring, B. Q.; Rizvi, I.; Evans, C. L.; Samkoe, K. S.; Verma, S.; Pogue, B. W.; Hasan, T. Imaging and Photodynamic Therapy: Mechanisms, Monitoring, and Optimization. *Chem. Rev.* **2010**, *110*, 2795−2838.

(10) Feng, W.; Chen, L.; Qin, M.; Zhou, X.; Zhang, Q.; Miao, Y.; Qiu, K.; Zhang, Y.; He, C. Flower-Like Pegylated MoS$_2$ Nanoflakes for Near-Infrared Photothermal Cancer Therapy. *Sci Rep.* **2015**, *5*, No. 17422.

(11) Lan, G.; Ni, K.; Lin, W. Nanoscale Metal−Organic Frameworks for Phototherapy of Cancer. *Coord. Chem. Rev.* **2019**, *379*, 65−81.

(12) Yang, B.; Chen, Y.; Shi, J. Reactive Oxygen Species (ROS)-Based Nanomedicine. *Chem. Rev.* **2019**, *119*, 4881−4985.

(13) Zhu, H.; Li, J.; Qi, X.; Chen, P.; Pu, K. Oxygenic Hybrid Semiconducting Nanoparticles for Enhanced Photodynamic Therapy. *Nano Lett.* **2018**, *18*, 586−594.

(14) Liu, X.; Su, H.; Shi, W.; Liu, Y.; Sun, Y.; Ge, D. Functionalized Poly (Pyrrole-3-Carboxylic Acid) Nanoneedles for Dual-Imaging Guided PDT/PTT Combination Therapy. *Biomaterials* **2018**, *167*, 177−190.

(15) Bian, H.; Ma, D.; Zhang, X.; Xin, K.; Yang, Y.; Peng, X.; Xiao, Y. Tailored Engineering of Novel Xanthonium Polymethine Dyes for Synergetic PDT and PTT Triggered by 1064 nm Laser toward Deep-Seated Tumors. *Small* **2021**, *17*, No. 2100398.

(16) Younis, M. R.; Wang, C.; An, R.; Wang, S.; Younis, M. A.; Li, Z.-Q.; Wang, Y.; Ihsan, A.; Ye, D.; Xia, X.-H. Low Power Single Laser Activated Synergistic Cancer Phototherapy Using Photosensitizer Functionalized Dual Plasmonic Photothermal Nanoagents. *ACS Nano* **2019**, *13*, 2544−2557.

(17) Taratula, O.; Doddapaneni, B. S.; Schumann, C.; Li, X.; Bracha, S.; Milovancev, M.; Alani, A. W. G.; Taratula, O. Naphthalocyanine-Based Biodegradable Polymeric Nanoparticles for Image-Guided Combinatorial Phototherapy. *Chem. Mater.* **2015**, *27*, 6155−6165.

(18) Feng, G.; Liu, B. Multifunctional AIEgens for Future Theranostics. *Small* **2016**, *12*, 6528−6535.

(19) Kumar, R.; Shin, W. S.; Sunwoo, K.; Kim, W. Y.; Koo, S.; Bhuniya, S.; Kim, J. S. Small Conjugate-Based Theranostic Agents: An Encouraging Approach for Cancer Therapy. *Chem. Soc. Rev.* **2015**, *44*, 6670−6683.

(20) Li, X.; Schumann, C.; Albarqi, H. A.; Lee, C. J.; Alani, A. W. G.; Bracha, S.; Milovancev, M.; Taratula, O.; Taratula, O. A Tumor-Activatable Theranostic Nanomedicine Platform for NIR Fluorescence-Guided Surgery and Combinatorial Phototherapy. *Theranostics* **2018**, *8*, 767−784.

(21) Lovell, J. F.; Liu, T. W. B.; Chen, J.; Zheng, G. Activatable Photosensitizers for Imaging and Therapy. *Chem. Rev.* **2010**, *110*, 2839−2857.

(22) Li, X.; Kolemen, S.; Yoon, J.; Akkaya, E. U. Activatable Photosensitizers: Agents for Selective Photodynamic Therapy. *Adv. Funct. Mater.* **2017**, *27*, No. 1604053.

(23) Oar, M. A.; Serin, J. M.; Dichtel, W. R.; Fréchet, J. M. J.; Ohulchanskyy, T. Y.; Prasad, P. N. Photosensitization of Singlet Oxygen via Two-Photon-Excited Fluorescence Resonance Energy Transfer in a Water-Soluble Dendrimer. *Chem. Mater.* **2005**, *17*, 2267−2275.

(24) Shan, J.; Budijono, S. J.; Hu, G.; Yao, N.; Kang, Y.; Ju, Y.; Prud'homme, R. K. Pegylated Composite Nanoparticles Containing Upconverting Phosphors and Meso-Tetraphenyl Porphine (TPP) for Photodynamic Therapy. *Adv. Funct. Mater.* **2011**, *21*, 2488−2495.

(25) Chen, X.; Lee, D.; Yu, S.; Kim, G.; Lee, S.; Cho, Y.; Jeong, H.; Nam, K. T.; Yoon, J. *In Vivo* Near-Infrared Imaging and Phototherapy of Tumors Using a Cathepsin B-Activated Fluorescent Probe. *Biomaterials* **2017**, *122*, 130−140.

(26) Yan, C.; Zhang, Y.; Guo, Z. Recent Progress on Molecularly Near-Infrared Fluorescent Probes for Chemotherapy and Photo-therapy. *Coord. Chem. Rev.* **2021**, *427*, No. 213556.

(27) Chen, H.; Khemtong, C.; Yang, X.; Chang, X.; Gao, J. Nanonization Strategies for Poorly Water-Soluble Drugs. *Drug Discovery Today* **2011**, *16*, 354−360.

(28) Lucky, S. S.; Soo, K. C.; Zhang, Y. Nanoparticles in Photodynamic Therapy. *Chem. Rev.* **2015**, *115*, 1990−2042.

(29) Feng, G.; Liu, B. Aggregation-Induced Emission (AIE) Dots: Emerging Theranostic Nanolights. *Acc. Chem. Res.* **2018**, *51*, 1404−1414.

(30) Zhang, Y.; Shi, M.; Yan, Z.; Zhang, S.; Wang, M.; Xu, H.; Li, H.; Ying, Y.; Qiu, S.; Liu, J.; Yang, H.; Chen, H.; He, H.; Guo, Z. Ultrastable Near-Infrared Nonlinear Organic Chromophore Nano-particles with Intramolecular Charge Transfer for Dually Photo-induced Tumor Ablation. *Adv. Healthcare Mater.* **2020**, *9*, No. 2001042.

(31) Maeda, H.; Wu, J.; Sawa, T.; Matsumura, Y.; Hori, K. Tumor Vascular Permeability and the EPR Effect in Macromolecular Therapeutics: A Review. *J. Controlled Release* **2000**, *65*, 271−284.

(32) Chari, R. V. J.; Miller, M. L.; Widdison, W. C. Antibody-Drug Conjugates: An Emerging Concept in Cancer Therapy. *Angew. Chem., Int. Ed.* **2014**, *53*, 3796−3827.

(33) Kanamala, M.; Wilson, W. R.; Yang, M.; Palmer, B. D.; Wu, Z. Mechanisms and Biomaterials in pH-Responsive Tumour Targeted Drug Delivery: A Review. *Biomaterials* **2016**, *85*, 152−167.

(34) Liu, Y.; Dai, R.; Wei, Q.; Li, W.; Zhu, G.; Chi, H.; Guo, Z.; Wang, L.; Cui, C.; Xu, J.; Ma, K. Dual-Functionalized Janus Mesoporous Silica Nanoparticles with Active Targeting and Charge Reversal for Synergistic Tumor-Targeting Therapy. *ACS Appl. Mater. Interfaces* **2019**, *11*, 44582−44592.

(35) Kong, F.; Liang, Z.; Luan, D.; Liu, X.; Xu, K.; Tang, B. A Glutathione (GSH)-Responsive Near-Infrared (NIR) Theranostic Prodrug for Cancer Therapy and Imaging. *Anal. Chem.* **2016**, *88*, 6450−6456.

(36) Liu, J.; Zhang, W.; Zhou, C.; Li, M.; Wang, X.; Zhang, W.; Liu, Z.; Wu, L.; James, T. D.; Li, P.; Tang, B. Precision Navigation of Hepatic Ischemia−Reperfusion Injury Guided by Lysosomal Viscosity-Activatable NIR-II Fluorescence. *J. Am. Chem. Soc.* **2022**, *144*, 13586−13599.

(37) Wu, W.; Mao, D.; Xu, S.; Ji, S.; Hu, F.; Ding, D.; Kong, D.; Liu, B. High Performance Photosensitizers with Aggregation-Induced Emission for Image-Guided Photodynamic Anticancer Therapy. *Mater. Horiz.* **2017**, *4*, 1110−1114.

(38) Tan, L.; He, C.; Chu, X.; Chu, Y.; Ding, Y. Charge-Reversal ZnO-Based Nanospheres for Stimuli-Responsive Release of Multiple Agents towards Synergistic Cancer Therapy. *Chem. Eng. J.* **2020**, *395*, No. 125177.

(39) Mo, C.; Wang, Z.; Yang, J.; Ouyang, Y.; Mo, Q.; Li, S.; He, P.; Chen, L.; Li, X. Rational Assembly of RGD/MoS$_2$/Doxorubicin Nanodrug for Targeted Drug Delivery, GSH-Stimulus Release and Chemo-Photothermal Synergistic Antitumor Activity. *J. Photochem. Photobiol., B* **2022**, *233*, No. 112487.

(40) Boedtkjer, E.; Pedersen, S. F. The Acidic Tumor Micro-environment as a Driver of Cancer. *Annu. Rev. Physiol.* **2020**, *82*, 103−126.

(41) Yang, T.; Liu, L.; Deng, Y.; Guo, Z.; Zhang, G.; Ge, Z.; Ke, H.; Chen, H. Ultrastable Near-Infrared Conjugated-Polymer Nano-particles for Dually Photoactive Tumor Inhibition. *Adv. Mater.* **2017**, *29*, No. 1700487.

(42) Zhang, J.; Yuan, Z.-F.; Wang, Y.; Chen, W.-H.; Luo, G.-F.; Cheng, S.-X.; Zhuo, R.-X.; Zhang, X.-Z. Multifunctional Envelope-Type Mesoporous Silica Nanoparticles for Tumor-Triggered Target-ing Drug Delivery. *J. Am. Chem. Soc.* **2013**, *135*, 5068−5073.